Catalytic oxidation of vinyl chloride emission over LaMnO$_3$ and LaB$_{0.2}$Mn$_{0.8}$O$_3$ (B = Co, Ni, Fe) catalysts

Chuanhui Zhang[a,b], Chao Wang[a], Wangcheng Zhan[a], Yanglong Guo[a,*], Yun Guo[a], Guanzhong Lu[a], Alexandre Baylet[b], Anne Giroir-Fendler[b,**]

[a] Key Laboratory for Advanced Materials and Research Institute of Industrial Catalysis, East China University of Science and Technology, Shanghai 200237, China
[b] Université Lyon 1, CNRS, UMR 5256, IRCELYON, Institut de recherches sur la catalyse et l'environnement de Lyon, 2 avenue Albert Einstein, 69626 Villeurbanne Cedex, France

ARTICLE INFO

ABSTRACT

The LaMnO$_3$ and LaB$_{0.2}$Mn$_{0.8}$O$_3$ (B = Co, Ni, Fe) perovskite-type oxides were prepared by the conventional co-precipitation method and studied as catalysts for the oxidation of vinyl chloride emission in the temperature range of 50–350 °C. Their physicochemical properties were characterized by ICP-AES, N$_2$ adsorption, XRD, H$_2$-TPR, O$_2$-TPD and XPS. Catalytic performances were evaluated for the oxidation of 1000 ppm of VC in air at a GHSV of 15,000 h^{-1}. The substituted LaB$_{0.2}$Mn$_{0.8}$O$_3$ samples showed higher catalytic activity than pure LaMnO$_3$. Characterization results revealed that the catalytic activity of the perovskite oxides was greatly related to the low-temperature reducibility of the B site and the amount of adsorbed oxygen species and vacancies on the surface. The surface adsorbed oxygen species played a key role in the catalytic reaction and oxygen vacancies promoted the oxygen mobility. A reaction mechanism of vinyl chloride oxidation over LaMnO$_3$-based perovskite oxides was proposed.

© 2012 Elsevier B.V. All rights reserved.

1. Introduction

In the industrial production process for polyvinyl chloride (PVC), large amounts of emission with low vinyl chloride (VC) concentration are released. As one of the chlorinated volatile organic compounds (CVOCs), VC is greatly harmful towards environment and public health. Due to the increasing stringent environmental regulations [1,2] to limit CVOCs emissions, it is becoming a troublesome task to clean such toxic and hazardous pollutants.

Catalytic oxidation is considered as an effective technology for CVOCs abatement and is widely applied. Lower operation temperature, high purifying efficiency and no secondary pollution make it more promising in the field of industrial emission purification. Among the catalysts used for the catalytic oxidation of CVOCs, transition and noble metals based catalysts [3–6] and molecular sieves [7,8] are commonly investigated by researchers. Pitkäaho et al. [9] studied the catalytic oxidation of dichloromethane (DCM) and perchloroethylene (PCE) over different alumina supported noble metal catalysts. They found that Pt-catalysts showed the best performances in DCM oxidation. In spite of high activity towards CVOCs oxidation over noble metals, high cost and deactivation easily caused by chlorine poisoning make it difficult to be applied in industrial processes. Molecular sieves with specific pore structures and tunable surface acid–base properties have received great interest in CVOCs decomposition. It has been previously found that various commercial H-zeolites (e.g. H-Y, H-ZSM-5 and H-MOR) showed high catalytic activity for the oxidation of 1, 2-dichloroethane (DCE) and trichloroethylene (TCE), correlated with presence of Brønsted acid sites [10–12]. Nevertheless, due to unstability of its structure and its acid sites, zeolite cannot stand the industrial hydrothermal conditions and becomes inactive at high temperature. In addition, the problem of the formation of polychlorinated by-products on these catalysts is yet to be solved. Nowadays, researchers are focusing more insight on transition metal oxides due to their relative high catalytic activity, lower preparation cost and good resistant ability for deactivation. Among the metal oxides, cobalt oxide, more specifically the Co$_3$O$_4$ crystalline phase, have been shown to be one of the most efficient materials for the total gas-phase oxidation of CVOCs [13,14]. Cerium based oxides, specifically ceria–zirconia mixed oxides, have attracted much attention for CVOCs abatement [15–17]. As reported, the high activity of cerium oxide has been attributed to its excellent oxygen storage capacity (OSC) and Ce^{4+}/Ce^{3+} redox properties [16,18,19]. Manganese oxide, supported or not, is another

important catalyst for the decomposition of CVOCs. It has been reported that the MnO_x–CeO_2 composite oxides showed high activity and stability in the catalytic combustion of trichloroethylene (TCE) and chlorobenzene (CB) [20,21]. In the last few decades, perovskite oxide with the general formula ABO_3 has been deeply investigated for CO oxidation [22], photocatalysis degradation of methyl orange [23], NO_x elimination [24] and VOCs abatement [25]. In perovskite structure, the A- and/or B-site cations could be substituted by another one without changing the structure. In this way, the oxidation states of the B cation and/or the amounts of non-stoichiometric oxygen could be modified, creating oxygen vacancies and improving catalytic activity. Among the ABO_3 materials, the lanthanum manganese perovskite oxide ($LaMnO_3$) shows high thermal stability and oxygen mobility, and it exhibits better activity in catalytic oxidation of numerous VOCs [26,27]. In 1990s, G. Wendt and C. Petit et al. studied this system for the abatement of different CVOCs [28–30]. The results showed that complete decomposition of CVOCs like C_1 (CH_3Cl, CH_2Cl_2, $CHCl_3$ and CCl_4) and C_2 (CCl_3–CH_3, CH_2Cl–CH_2Cl) molecules could be achieved in air below 550 °C. However, the formation of by-products such as C—C coupling, higher chlorinated and cracking compounds involved catalytic deactivation. Since, the $LaMnO_3$ perovskite-type catalysts are seldom investigated in the field of CVOCs abatement.

In this work, the $LaMnO_3$-based perovskite catalysts are prepared by co-precipitation method and investigated for the catalytic oxidation of vinyl chloride emission. Additionally, the effect of B-site substitution by Co, Ni and Fe on the catalyst physicochemical properties is studied by series of characterization techniques. Moreover, a catalytic reaction mechanism for VC oxidation on the catalyst surface is proposed.

2. Experimental

2.1. Catalyst preparation

$LaMnO_3$ and $LaB_{0.2}Mn_{0.8}O_3$ (B = Co, Ni, Fe) perovskite-type catalysts were prepared by co-precipitation method using metal nitrates as salt precursors which were mixed in aqueous solution at a desired stoichiometric ratio. A NaOH–Na_2CO_3 aqueous solution with a concentration of $2\,mol\,L^{-1}$ and $1\,mol\,L^{-1}$, respectively, was added dropwise to the previous solution, under magnetic stirring, allowing salt precursor precipitation. The pH was maintained between 10 and 11. After addition, the precipitate was left for 4 h at room temperature, filtered and thoroughly washed with deionized water. The precipitate was dried at 120 °C overnight in an oven and calcined at 750 °C for 2 h in a muffle furnace in order to obtain the perovskite phase. The calcined samples were grounded, tableted and sieved between 40 and 60 mesh size. In order to facilitate the presentation, the $LaMnO_3$ and $LaB_{0.2}Mn_{0.8}O_3$ (B = Co, Ni, Fe) catalysts were denoted as LMO, LCMO, LNMO and LFMO, respectively.

2.2. Catalytic activity test

The catalytic activity of the perovskite based catalyst was evaluated for the oxidation of VC. Catalytical test was carried out in a continuous flow fixed-bed quartz reactor with 12 mm I.D. at the atmospheric pressure. The catalyst (500 mg) was packed in the reactor and catalytic activity measurement was performed under the reaction conditions of 1000 ppm VC diluted by air, GHSV of $15,000\,h^{-1}$ and the reaction temperature range of 50–350 °C. Reaction temperature was monitored by a thermocouple placed in the middle of the catalyst bed. Flow rates were controlled by mass flow controllers (SevenStar). The composition of the gas effluent was analyzed by an online gas chromatograph equiped with a Col Elite-1 (60m × 0.32mm × 1.00 μm) capillary

column and a FID detector. Only HCl, CO_2 and H_2O products were detected. No by-products such as chlorohydrocarbons and chlorine were qualitatively identified by INFICON IPC400 quadrupole mass spectrometer. The VC conversion was calculated by Eq. (1) which was based on the concentration difference between the inlet and outlet.

$$X_{VC}(\%) = \frac{[VC]_{in} - [VC]_{out}}{[VC]_{in}} \times 100 \qquad (Eq.1)$$

2.3. Catalyst characterization

The catalyst chemical compositions were determined by inductively coupled-plasma atomic emission spectroscopy (ICP-AES) using a Varian 710-ES instrument. The specific surface areas (SSA) were measured by N_2 adsorption–desorption isotherms measured at 77 K on a NOVA 4200e Surface Area & Pore Size Analyzer. The Brunauer–Emmett–Teller (BET) method was used to calculate the specific surface area. Powder X-ray diffraction (XRD) measurements were performed on a BrukerAXS D8 Focus diffractometer with $CuK\alpha$ radiation (40 kV, 40 mA, λ = 1.5406 Å, scanning step = 0.02°) and the diffraction patterns were recorded in the range of $10 < 2\theta < 80°$ at the scanning rate of $6° \, min^{-1}$. Phase identification was carried out using MDI Jade 5.0 program compared with the JCPDF database cards. The cell refinement method in MDI Jade 5.0 program was used to refine the crystal structures and to calculate the unit-cell parameters. The catalyst redox behaviors were examined by hydrogen temperature programmed reduction (H_2-TPR). Experiments were conducted on a TP-5080 Auto Desorption instrument. Prior to each run, the sample (100 mg) was pre-treated in Ar stream at 200 °C for 30 min. After cooling down to room temperature, 5% H_2/N_2 mixture gas of $40\,mL\,min^{-1}$ was introduced and the reactor was heated at a temperature rate of $10 °C\,min^{-1}$ from room temperature to 900 °C and maintained at this temperature for 20 min. The thermal conductivity detector (TCD) response was calibrated thanks to a commercial CuO sample (SCR, 99.99%). The consumption of H_2 was quantitatively measured by time integration of the TPR profiles. Oxygen-temperature programmed desorption (O_2-TPD) measurements were conducted in a U-shaped quartz reactor and the desorption signal of oxygen was recorded with an online INFICON IPC400 quadrupole mass spectrometer. Prior to each test, the sample (100 mg) was pre-treated in a purified oxygen stream at 550 °C for 60 min, cooled down to room temperature in oxygen atmosphere and purged by a stream of purified He until stabilization of MS base line. The reactor was heated at a temperature rate of $20 °C\,min^{-1}$ from room temperature to 1000 °C. Simultaneously, the desorbed oxygen signal was collected by the MS detector. X-ray photoelectron spectroscopy (XPS) spectra were recorded on a Thermo ESCALAB 250 electron spectrometer with a monochromatized AlK_α X-ray source (1486.6 eV) and a passing energy of 20 eV. C_{1s} (binding energy 284.8 eV) of adventitious carbon was used as the reference. XPS spectra were deconvoluted using XPSPEAK 41 program by the curve fitting after the Shirley-type background subtraction.

3. Results and discussion

3.1. Elemental analysis, specific surface areas and XRD characterization

Chemical compositions, specific surface areas (SSA), crystal symmetry and unit-cell parameters of the calcined samples are summarized in Table 1 and their XRD patterns are shown in Fig. 1. Within experimental and apparatus error, the determined molecular formulae (LMO, LCMO and LNMO samples) were close to the nominal one. However, for the LFMO sample, the experimental

Table 1
Physical properties of LaMnO$_3$ and LaB$_{0.2}$Mn$_{0.8}$O$_3$ (B = Co, Ni, Fe) catalysts.

Catalyst	Chemical composition[a]	SSA[b] (m^2 g^{-1})	Symmetry[c]	Unit-cell parameters[c]		
				a (Å)	b (Å)	c (Å)
LMO	La$_{1.01}$Mn$_{0.99}$O$_{3+/-\delta}$	14	Rhombohedral R-3c	5.4933	5.4933	13.3246
LCMO	La$_{1.01}$Mn$_{0.81}$Co$_{0.18}$O$_{3+/-\delta}$	11	Rhombohedral R-3c	5.4722	5.4722	13.3861
LNMO	La$_{1.01}$Mn$_{0.80}$Ni$_{0.19}$O$_{3+/-\delta}$	22	Rhombohedral R-3c	5.4705	5.4705	13.3497
LFMO	La$_{1.02}$Mn$_{0.75}$Fe$_{0.23}$O$_{3+/-\delta}$	25	Rhombohedral R-3c	5.4874	5.4874	13.3519

[a] Determined by ICP-AES analysis.
[b] Measured by N$_2$ adsorption (BET method).
[c] Determined and calculated from XRD patterns (MDI Jade 5.0 program).

iron amount was higher and the manganese amount was lower than the theoretical values, La$_{1.02}$Mn$_{0.75}$Fe$_{0.23}$O$_{3+/-\delta}$ and LaMn$_{0.80}$Fe$_{0.20}$O$_{3+/-\delta}$, respectively. As expected for perovskite materials, due to lack of internal porosity and high temperature calcination, all samples had relatively low specific surface areas. The LNMO and LFMO samples had higher surface areas (22 and 25 m^2 g^{-1}, respectively) than the LMO sample (14 m^2 g^{-1}). The Co substituted sample (LCMO) presented the lowest SSA value (11 m^2 g^{-1}). Pure and well crystallized perovskite phases were obtained after calcination at 750 °C for 2 h. The diffraction peaks of impurities such as lanthanum oxide La$_2$O$_3$ (JCPDS PDF#22–369 and #24–554) or lanthanum oxycarbonate (LaO)$_2$CO$_3$ (JCPDS #23-320, #23-322 and #22-1127) were not detected. As shown in Fig. 1, the diffraction peaks at 2θ = 23.1°, 32.6°, 40.3°, 47.0°, 53.1°, 58.4°, 68.3° and 77.8° were correlated with those of the LaMnO$_{3.26}$ structure (JCPDS #50-0299), which indicated that the four samples prepared had rhombohedral perovskite-type structure (space group R-3c). Similar results were reported previously by Alonso [31] and Song [32].

3.2. Redox properties

Redox properties of the different perovskite samples were evaluated by H$_2$-TPR. The corresponding TPR profiles are displayed in Fig. 2. For each sample, two main reduction regions were observed, the first one in the temperature range of 150–550 °C and the second one in the temperature range of 600–850 °C. Moreover, a small shoulder centered in the temperature range of 150–250 °C

appeared (Fig. 2A). This phenomenon could be assigned to the removal of oxygen adspecies on the surface. Complete reduction of Mn^{2+} cation to metallic manganese does not happen in the reduction process of manganese oxides [33–35]. For the unsubstituted LMO sample, the reduction peak between 250 and 550 °C could be correlated to the reduction of Mn^{4+} to Mn^{3+}, whereas the one
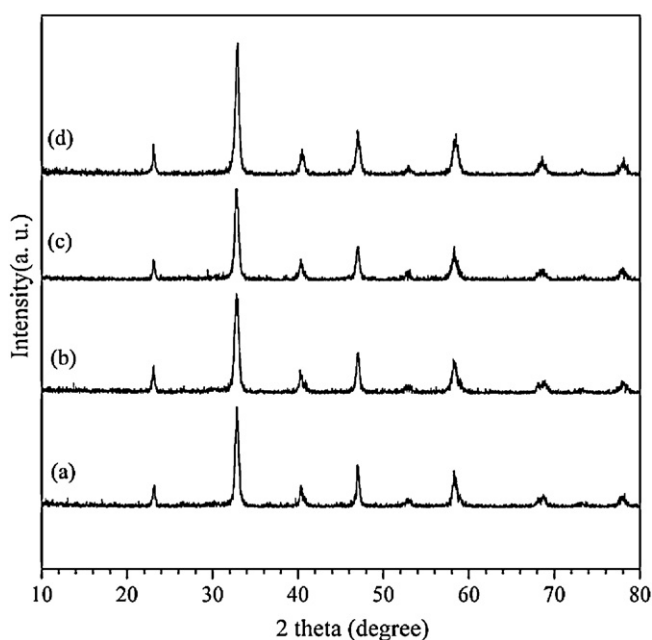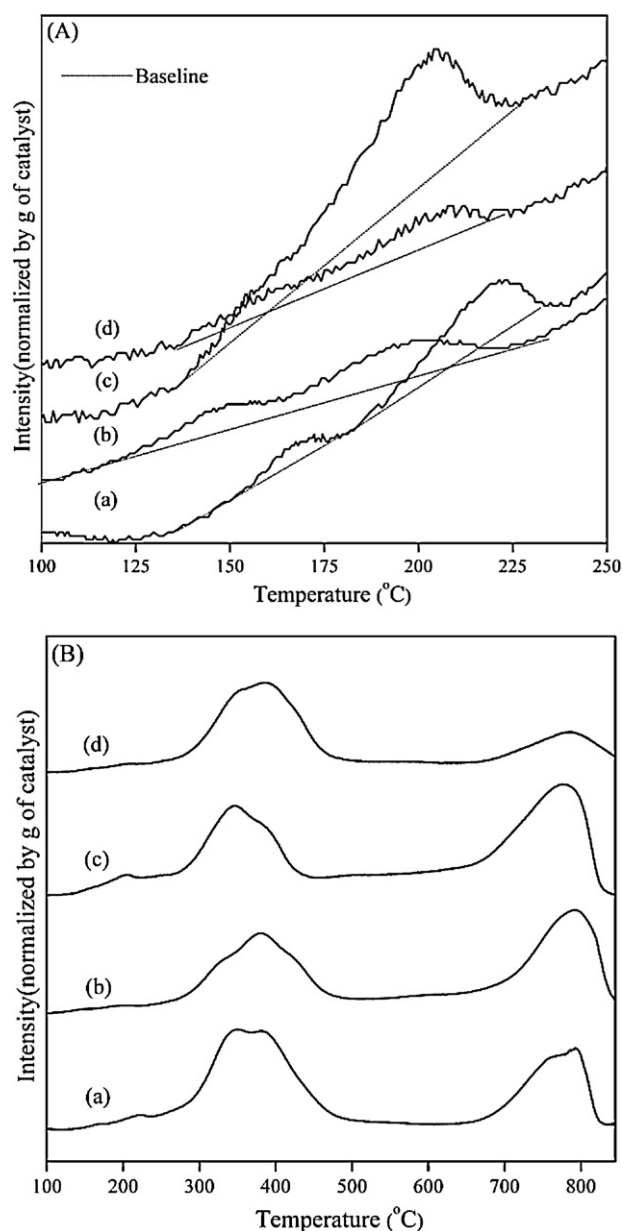

Fig. 2. H$_2$-TPR profiles (a) LMO (b) LCMO (c) LNMO and (d) LFMO in (A) low temperature range and (B) overall temperature range.

Fig. 1. XRD patterns of (a) LMO (b) LCMO (c) LNMO and (d) LFMO.

Table 2
Reducibility properties of $LaMnO_3$ and $LaB_{0.2}Mn_{0.8}O_3$ (B = Co, Ni, Fe) catalysts.

Catalyst	[0,2-5]H_2 consumption (mmol g^{-1} cat.)			Total
	T^a < 250	$250 \leq T^a$ < 550	$T^a \leq 600$	
LMO	0.28	1.33(383)[b]	0.95(786)	2.56
LCMO	0.33	1.30(380)	1.38(790)	3.01
LNMO	0.37	1.37(347)	1.43(778)	3.17
LFMO	0.22	1.46(382)	0.81(786)	2.49

[a] Temperature (°C).
[b] The temperature of peak maximum are presented in brackets.

above 600 °C was associated with the reduction of Mn^{3+} to Mn^{2+} [35]. For the substituted samples, with the same B-site substitution ratio, the presence of Co, Ni and Fe modified slightly the reduction behavior. For the LCMO, LNMO and LFMO samples, in the temperature range of 250–550 °C, the reduction of Co^{3+} to Co^{2+}, Ni^{3+} to Ni^{2+} and Fe^{4+} to Fe^{3+} as well as a successive reduction of Fe^{3+} to Fe^{2+} was considered to occur simultaneously with the reduction of Mn^{4+} to Mn^{3+} [35–37]. For the LCMO and LNMO samples, besides the reduction of Mn^{3+} to Mn^{2+}, the reduction of Co^{2+} to metallic cobalt and Ni^{2+} to metallic nickel contributed to the high temperature reduction peak (above 600 °C). It was reported that Fe^{2+} was difficult to be reduced into metallic iron in the Fe-based perovskite [38]. For the LFMO sample, a minor reduction peak at high temperature could be observed, indicating that a low contribution was due to the reduction of Fe^{2+}. Through quantitative analysis of the H_2-TPR profiles, the H_2 consumption of all samples are summarized in Table 2. For all samples, the H_2 consumption as a function of the temperature was (i) between 0.22 and 0.37 mmol g^{-1} for temperature below 250 °C, (ii) between 1.24 and 1.46 mmol g^{-1} at intermediate temperature (250–550 °C) and (iii) between 0.81 and 1.43 mmol g^{-1} for temperature above 600 °C. It could be inferred that the amounts of surface oxygen adspecies followed the sequence LNMO > LCMO > LMO > LFMO according to the H_2 consumption below 250 °C. Apparently, H_2 consumption of the LFMO and LNMO samples at intermediate temperature (250–550 °C) was much larger than that of the LMO sample, whereas that for LCMO, the H_2 consumption was the smallest. As remark, the samples with higher specific surface areas consumed larger amounts of H_2 during this reduction process. Moreover, if the manganese, cobalt, nickel and iron cations in the perovskite samples were totally presented as Mn^{4+}, Co^{3+}, Ni^{3+} and Fe^{4+} and then completely reduced into Mn^{2+}, Co^0, Ni^0 and Fe^{2+} during the whole reduction process, the theoretical H_2-consumption of each sample, which was calculated on the basis of the chemical formula determined by ICP-AES analysis, would be 4.08, 4.37, 4.44 and 4.02 mmol g^{-1} for the LMO, LCMO, LNMO and LFMO samples, respectively. However, the total H_2 consumption was between 2.49 and 3.17 mmol g^{-1}, indicating that multivalent metal ions in the form of Mn^{4+}/Mn^{3+}, Co^{3+}/Co^{2+}, Ni^{3+}/Ni^{2+} and Fe^{4+}/Fe^{3+} would coexist in all the perovskite samples. From the temperature of the peak maximum presented in Table 2, there were slight differences for the LMO, LCMO and LFMO samples. However, the temperature of the peak maximum was lower for the LNMO sample, illustrating that LNMO exhibited an easier reducibility behavior among all samples.

3.3. Surface analysis by XPS

The La_{3d}, Mn_{2p}, O_{1s}, Co_{2p}, Ni_{2p}, Fe_{2p}, and C_{1s} XPS spectra of all samples were recorded. The integration of the corresponding peaks allowed to determine the atomic ratios of surface species which were collected in Table 3. From these results, the surface La/Mn ratio of all samples were higher than the nominal La/Mn atomic ratio, equal to 1 for LMO sample and equal to 1.25 for LCMO, LNMO and LFMO samples, indicating a La surface enrichment. The similar phenomenon is found in [39,40]. Despite the surface La enrichment, XRD analysis did not reveal the presence of diffraction peaks attributed to lanthanum oxide (La_2O_3) or lanthanum oxycarbonate (($LaO)_2CO_3$). This could be due to the low quantity of those species on the sample surface. Fig. 3 shows the La_{3d}, Mn_{2p} and O_{1s} XPS spectra of the LMO, LCMO, LNMO and LFMO samples. The La_{3d} XPS spectrum was displayed in Fig. 3A. The peaks of La $3d_{5/2}$ and La $3d_{3/2}$ were located at 834.0 eV and 838.3 eV and at 850.8 eV and 855.4 eV, respectively. The spin-orbit splitting of La 3d level is 16.8 eV and is identical for all samples. These values observed for the perovskites were close to the values of pure lanthanum oxide (La_2O_3) given by Connell et al., 834.4 eV for La $3d_{3/2}$ and 838.0 eV for $3d_{5/2}$ [41], indicating that lanthanum ions were present in the trivalent state. The existence of Mn^{4+} and Mn^{3+} species in $LaMnO_3$ perovskite-type catalysts were commonly reported [39,40,42]. In Fig. 3B, there were two asymmetrical peaks located at 642.1 ($Mn2p_{3/2}$) and 653.5 eV ($Mn2p_{1/2}$). $Mn2p_{3/2}$ and $Mn2p_{1/2}$ peaks could be deconvoluted into two peaks at 641.5 and 642.9 eV and at 653.0 and 654.5 eV, respectively. The peaks located at 641.5 and 653.0 eV are assigned to Mn^{3+} ions, while the peaks located at 642.9 and 654.5 eV are assigned to Mn^{4+} ions [42,43]. Thanks to quantitative analysis, the molar ratio of Mn^{4+}/Mn^{3+} on the surface was determined and summarized in Table 3. A difference in surface Mn^{4+}/Mn^{3+} molar ratio was observed between the different samples and followed the sequence LNMO > LCMO > LFMO > LMO from the highest to the lowest ratio. Thus the substitution of B-site over the $LaMnO_3$ perovskites influenced the surface concentration of Mn^{4+}. In Fig. 3C, there were three oxygen signals located at 529.4, 531.1, and 532.8 eV attributed to lattice oxygen O_{latt} (O^{2-}), surface absorbed oxygen O_{ads} (O^-, O_2^- or O_2^{2-}) and oxygen-containing groups such as hydroxyl and/or carbonate species on the surface, respectively [21,44,45]. The molar ratio of O_{ads}/O_{latt} was obtained thanks to quantitative calculation of the corresponding peaks areas and is shown in Table 3. The molar ratio of O_{ads}/O_{latt} followed the same sequence as that of Mn^{4+}/Mn^{3+}. Among the calcined samples, the LNMO sample exhibited the

Table 3
XPS-derived surface compositions of $LaMnO_3$ and $LaB_{0.2}Mn_{0.8}O_3$ (B = Co, Ni, Fe).

Catalyst	La/Mn atomic ratio	B/Mn atomic ratio	Mn/(La + B + Mn) atomic ratio	O_{ads}/O_{latt} molar ratio	Mn^{4+}/Mn^{3+} molar ratio
LMO	1.465 (1.0)[a]	–	0.406 (0.5) [a]	1.008	0.975
LCMO	1.584 (1.25)	0.138 (0.25) [a]	0.367 (0.4)	1.071	1.115
LNMO	1.427 (1.25)	0.143 (0.25)	0.389 (0.4)	1.104	1.216
LFMO	1.662 (1.25)	0.148 (0.25)	0.356 (0.4)	1.010	1.081

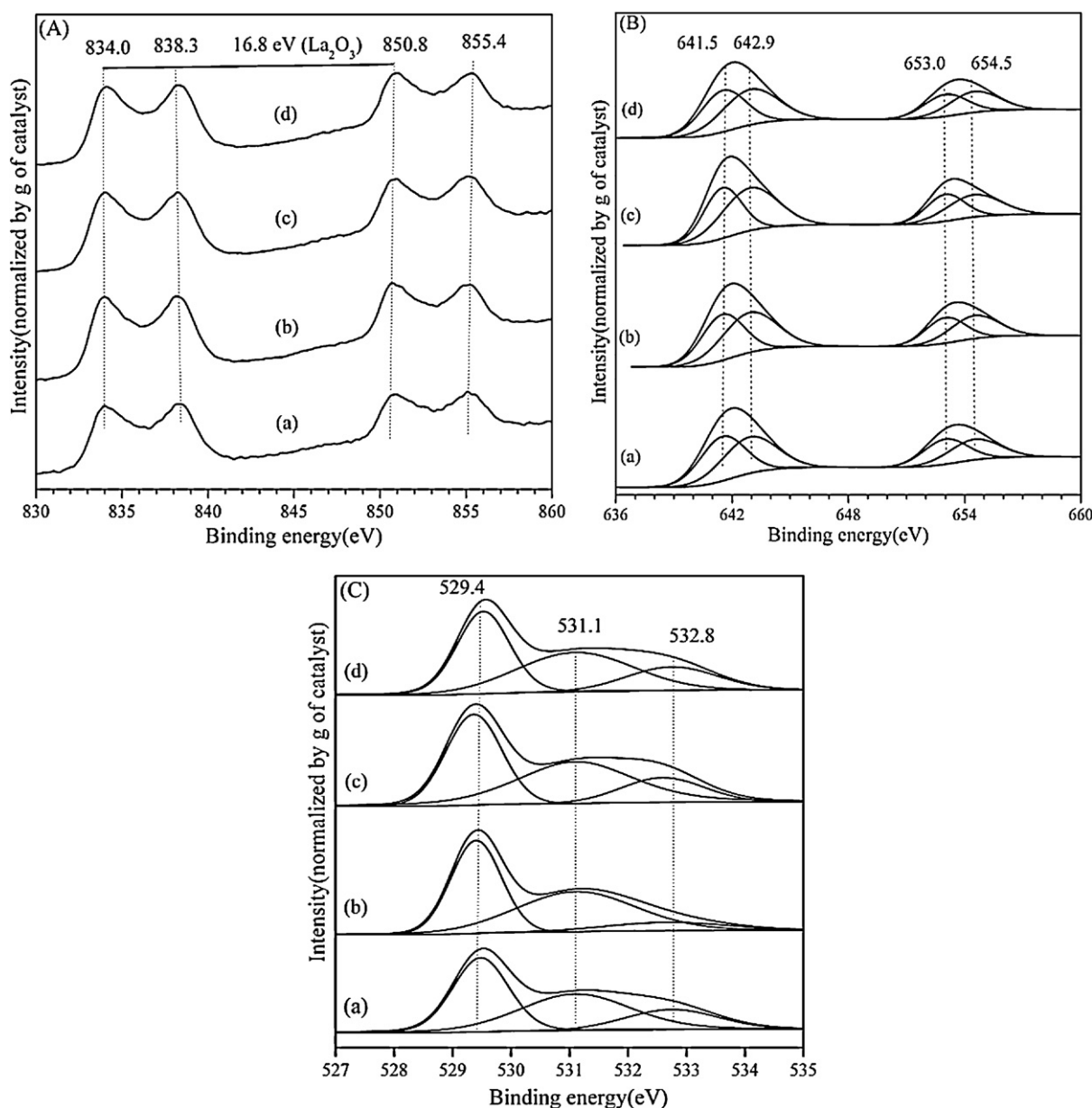[a] The data in brackets are the nominal compositions of $LaMnO_3$ and $LaB_{0.2}Mn_{0.8}O_3$ (B = Co, Ni, Fe).

Fig. 3. (A) La$_{3d}$, (B) Mn$_{2p}$ and (C) O$_{1s}$ XPS spectra of (a) LMO, (b) LCMO, (c) LNMO and (d) LFMO.

highest O$_{ads}$/O$_{latt}$ molar ratio and this result was in agreement with the result obtained in the H$_2$-TPR study.

3.4. Surface and bulk oxygen species

O$_2$-TPD measurements were performed in order to investigate the surface and bulk oxygen species of the perovskite samples. The oxygen desorption profiles within the temperature range of 200–900 °C are depicted in Fig. 4. For the LMO sample, obviously no oxygen desorption occurred before 400 °C and the desorption began very slowly with the temperature increasing. At 750 °C, a very intense peak appeared with an overlapping shoulder around 615 °C. For the LCMO, LNMO and LFMO samples, three oxygen desorption regions in the temperature range of 220–440 °C, 440–720 °C and 720–900 °C were observed. The oxygen species desorbed in the first region, denoted as O$_\alpha$, could be ascribed to the weakest molecular physisorbed and/or chemisorbed oxygen on the surface [46,47]. In this region, a wide range of peak around 315 °C for the LCMO sample and a doublet peaks at 295 and 410 °C for the

LNMO sample could be observed whereas only one or two small and unobvious peaks for the LFMO sample appeared. The oxygen species desorbed in the second region, denoted as O$_\beta$, could be ascribed to the oxygen originating from the oxygen vacancies on the surface or in the subsurface [37]. In this region, different peaks could be observed depending on the sample, (i) a small peak at 495 °C and an intense one at 665 °C for the LCMO sample, (ii) three continuous peaks at 498, 582 and 680 °C for the LNMO sample and (iii) an intense peak at 660 °C for the LFMO sample. The oxygen species desorbed in the higher temperature region, denoted as O$_\gamma$, could be ascribed to the oxygen originating from the crystal lattice of the perovskite oxides [37]. Oxygen vacancies were considered as the exchange and transformation media between the molecular oxygen on the surface and the lattice oxygen in the crystal structure. Consequently, the amounts of O$_\beta$ could be a reflection of the oxygen vacancies from the surface or the subsurface of the samples. The amounts of O$_\beta$ was obtained by quantitative integration of the peaks in the temperature range of 440–720 °C. The catalyst ranking based on the O$_\beta$ amount from the highest to the
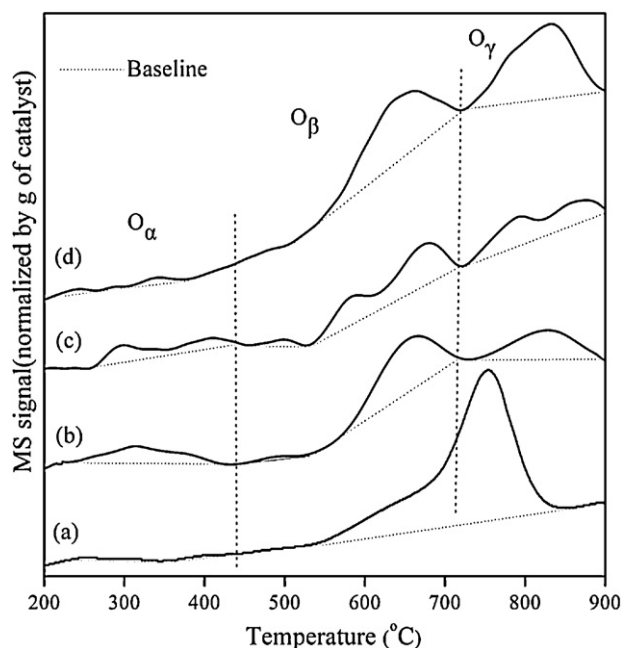
Fig. 4. O_2-TPD profiles of (a) LMO (b) LCMO (c) LNMO and (d) LFMO.

lowest is LNMO > LCMO > LFMO > LMO. The result indicated that more oxygen vacancies were generated when the B site in the LaMnO$_3$ perovskite structure was substituted by Co, Ni or Fe. Among these samples, Ni element has the most outstanding effect.

3.5. Catalytic performance and relationship with characterization results

The catalytic behaviors of the LaMnO$_3$ and LaB$_{0.2}$Mn$_{0.8}$O$_3$ (B = Co, Ni, Fe) catalysts for the complete oxidation of VC were evaluated. The results of VC conversion as a function of the reaction temperature are shown in Fig. 5. T$_{50}$ and T$_{90}$, corresponding to the temperatures at 50% and 90% of VC conversion, are summarized in Table 4. From the curves on Fig. 5 and the values in Table 4, the LNMO sample exhibited the highest catalytic
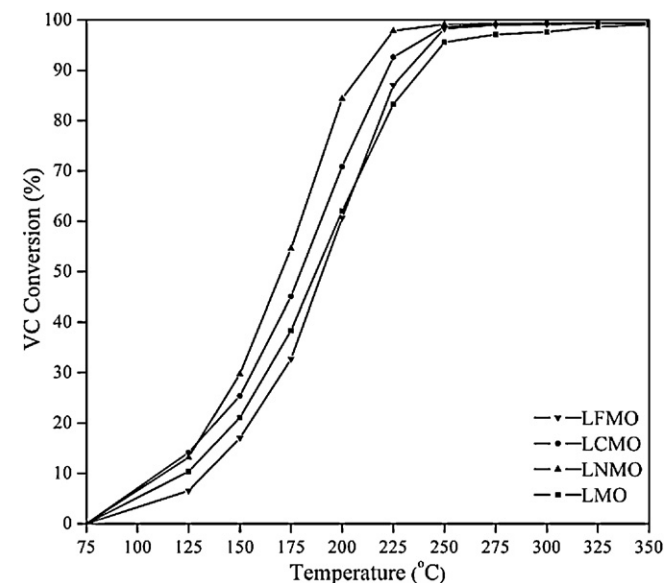

Fig. 5. VC conversion as a function of the reaction temperature over LaMnO$_3$ and LaB$_{0.2}$Mn$_{0.8}$O$_3$ (B = Co, Ni, Fe) catalysts.

activity for VC oxidation. The T$_{50}$ and T$_{90}$ values were 168 and 210 °C, respectively, values being 20 and 30 °C lower than those observed for LMO sample. The LCMO sample also showed relatively higher catalytic activity, with T$_{50}$ and T$_{90}$ values of 10 and 15 °C lower than that of LMO. The LFMO sample exhibited the poorer activity at the lower temperature (below 200 °C) compared with the LMO sample. However, with the temperature increasing (above 200 °C), the VC conversion straightened up faster over LFMO than LMO. The catalyst ranking in terms of catalytic activity, from the lowest to highest T$_{50}$ and T$_{90}$ values, is as follows LNMO > LCMO > LFMO > LMO, revealing that the addition of different metals into the perovskite structure improved the catalytic performance for the complete oxidation of VC. To deeply investigate the VC oxidation reaction, an INFICON IPC400 mass spectrometer was used in order to identify the reaction products. At 300 °C or above, VC was completely decomposed into HCl, CO$_2$ and H$_2$O and no by-products such as chlorohydrocarbons and chlorine were detected.

It is generally considered that some factors such as morphology (including microstructure, crystalline phase and specific surface area), redox properties (including the low-temperature reducibility and the nature of the redox couple) and surface chemical species (including adsorbed oxygen, the amount of B-site cations or oxygen vacancies) dominate the catalytic activity of LaMnO$_3$ perovskite-type materials in the oxidation reaction. With the aim to improve the catalytic performances, a lot of researchers focused their efforts on understanding those effects. For example, Hongxing Dai et al. prepared LaMnO$_3$ three-dimensionally ordered macroporous (3DOM) perovskite using templating method with the assistance of surfactant [48]. The surfactant influenced the pore structure of LaMnO$_3$ material and allowed to obtain high surface area (37–39 m^2 g^{-1}). Results showed that the catalytic performance of porous LaMnO$_3$ sample was superior to the bulk counterpart for toluene oxidation. In order to enhance redox properties, the B-site substituted LaMnO$_3$ perovskite with palladium, platinum and rhodium was studied for methanol partial oxidation by Lin et al.[49]. Authors showed that significant promotion of reducibility and oxygen activity were achieved for LaMn$_{0.95}$B$_{0.05}$O$_3$ compared to the untainted LaMnO$_3$ catalysts. Consequently, the LaMn$_{0.95}$B$_{0.05}$O$_3$ exhibited higher reactivity than pure LaMnO$_3$.

In this work, the conventional co-precipitation method was used in order to prepare LaMnO$_3$ and LaB$_{0.2}$Mn$_{0.8}$O$_{3+-/\delta}$ samples. From XRD and BET results, no significant morphology differences were observed between the samples. Moreover, there was no evident correlation between the specific surface area and the catalytic activity. Indeed, the LFMO sample had the highest specific surface area but showed poorer catalytic activity than the LCMO sample, which had the lowest specific surface area. Thus, the specific surface area did not influence the catalytic activity for VC oxidation.

From the results of H$_2$-TPR, O$_2$-TPD and XPS analysis, the addition of Co, Ni and Fe had significant effect on the redox properties and surface species of LaMnO$_3$ perovskite oxides, dominating the catalytic reactivity for VC oxidation. From H$_2$-TPR profiles (Fig. 2) and H$_2$ quantification (Table 2), the total H$_2$ consumption in the low temperature range (150–550 °C) for the reduction of the oxygen adspecies and the different redox couples,

Table 4
Temperature at 50 and 90% of VC conversion of LaMnO$_3$ and LaB$_{0.2}$Mn$_{0.8}$O$_3$ (B = Co, Ni, Fe) catalysts.

Catalysts	T_{50} (°C)	T_{90} (°C)
LMO	188	240
LCMO	178	225
LNMO	168	210
LFMO	190	232

such as Mn^{4+}/Mn^{3+}, Co^{3+}/Co^{2+}, Ni^{3+}/Ni^{2+}, Fe^{4+}/Fe^{3+} and Fe^{3+}/Fe^{2+}, increased for all the substituted samples. The perovskite ranking based on the H_2 consumption from the highest to the lowest value is as follows LNMO ($1.74\,mmol\,g^{-1}$) > LFMO ($1.68\,mmol\,g^{-1}$) > LCMO ($1.63\,mmol\,g^{-1}$) > LMO ($1.61\,mmol\,g^{-1}$). Specifically for the LNMO sample, the maximum of the reduction peak was shifted to lower temperature, indicating a reducibility enhancement. This sample also exhibited the highest catalytic activity for VC oxidation. On contrary, the LFMO sample had smaller amounts of oxygen adspecies than that of other samples and exhibited poorer catalytic activity for VC oxidation at low temperature (below 210 °C), as shown in Fig. 5. From the O_2-TPD study, for the substituted samples, more desorbed O_β species appeared, indicating that more oxygen vacancies were generated and participated in the oxygen migration process. Due to the increase of oxygen vacancies, the catalytic performance of the substituted samples was superior to that of the unsubstitued LMO sample for VC oxidation.

It has been reported that the variable oxidation state of B site cations was one component for the catalytic activity [50]. For the $AB_{1-x}B'_xO_3$ perovskite oxide, the redox couple could be $B^{n+}/B^{(n-1)+}$ and/or $B'^{n+}/B'^{(n-1)+}$. However, it was concluded that the $B'^{n+}/B'^{(n-1)+}$ couple played the main role during catalytic reaction if high activity was obtained at high amount of B' cation (i.e. $x > 0.5$). For all samples prepared in this study, Mn^{4+}/Mn^{3+} is the main redox couple and the substitution of the B cation could modify the oxidation state of Mn cation and/or the amount of non-stoichiometric oxygen. From the XPS results, it was revealed that the molar ratio of Mn^{4+}/Mn^{3+} on the surface increased when the LMO sample was substituted with Co, Ni and Fe. Moreover, another observation from the XPS analysis was that the relative molar ratio of O_{ads}/O_{latt} increased with the B-site substitution. It is generally assumed that the surface adsorbed oxygen was the most active species in catalytic oxidation reactions, especially for the low-temperature oxidation reaction. The amount of adsorbed oxygen species governed the overall reaction rate on the catalyst surface. In this work, the substituted samples with higher O_{ads} concentration showed higher catalytic activity than the LMO sample.

To conclude, in the $LaMnO_3$ perovskite oxide, Mn^{4+}/Mn^{3+} redox couple played the main role in the catalytic oxidation of VC. B-site substitution with Co, Ni and Fe (i) generated more Mn^{4+} species (ii) enhanced the redox ability of Mn^{4+}/Mn^{3+} couple, (iii) created more oxygen vacancies, increasing the oxygen mobility and involving more adsorbed oxygen species, which are considered as the most active species for the catalytic oxidation reaction. Finally, the improved catalytic performance of the substituted samples for VC oxidation was achieved.

In the research field of oxidation reactions over perovskite oxides, Voorhoeve et al. proposed two types of oxidation mechanism [51]. The first one was intrafacial reactions in which lattice oxygens act as the active species and the second one was suprafacial reactions in which adsorbed oxygen act as the active species. The suprafacial mechanism was assumed to prevail in the low temperature range, at which an adsorption–desorption equilibrium of oxygen was thermodynamically maintained. With the temperature increasing, the concentration of surface adsorbed oxygen decreased and the lattice oxygen became more mobile and participated in the oxidation reactions, which implied a gradual transition from the suprafacial mechanism to the intrafacial mechanism. Barbero et al. studied the combustion of ethanol and n-hexane over $La_{1-x}Ca_xMnO_3$ ($x = 0$, 0.1, 0.2, 0.3) perovskite catalysts and suggested that both the ethanol and n-hexane combustion reactions occured by means of a suprafacial reaction mechanism in which the adsorbed oxygen species played a predominant role [27].

In this present study, the complete conversion of VC occurred below 300 °C over the $LaMnO_3$ and $LaB_{0.2}Mn_{0.8}O_3$ (B = Co, Ni, Fe) catalysts, suggesting that the combustion of VC proceeded via the suprafacial mechanism. From the catalytic test and characterizations, it can be assumed that adsorbed oxygen was the dominant oxygen specie participating in this reaction and the amount of original adsorbed oxygen on the surface could influence the initial reaction rate at low temperature. Moreover, with the adsorbed oxygen consumed, oxygen vacancies played a key role in oxygen stabilization, activation and migration. The activated oxygen desorbed from oxygen vacancies migrated to the surface, became the complement of consumed adsorbed oxygen and favored the continuous oxidation of VC at higher temperature. This suprafacial mechanism for VC oxidation suggest that (i) higher the adsorbed oxygen concentration on the surface, higher the initial reaction rate and lower the ignition temperature, (ii) more oxygen vacancies were created being a media for oxygen activation and enhancing the oxygen mobility. Such species were favorable for the VC oxidation at higher temperature.

4. Conclusion

$LaMnO_3$ and $LaB_{0.2}Mn_{0.8}O_3$ (B = Co, Ni, Fe) catalysts were prepared by co-precipitation method and evaluated for the catalytic oxidation of vinyl chloride (VC). For all the samples, XRD patterns showed the formation of rhombohedral perovskite-type structures. The substitution of Co, Ni and Fe increased the amounts of Mn^{4+} and adsorbed oxygen species on the catalyst surface. The catalyst ranking in terms of O_{ads} quantity from the highest to the lowest is LNMO > LCMO > LFMO > LMO. Higher catalytic activity for VC oxidation was achieved thanks to B-site substitution. The LNMO sample showed the best catalytic performance ($T_{50} = 168$ °C and $T_{90} = 210$ °C) for the abatement of 1000 ppm of VC in air at a GHSV of $15,000\,h^{-1}$. The catalytic activity enhancement of the B-site substituted perovskite was related to the lower reducibility temperature, the large amount of surface adsorbed oxygen and higher oxygen mobility.

Acknowledgements

References

[1] J. Fenger, Atmospheric Environment 43 (2009) 13–22.
[2] Thematic Strategy on Air Pollution, Communication from the Commission to the Council and The European Parliament, Commission of the European Communities, COM (2005) 446 final, Brussels, 2005.
[3] M. Taralunga, B. Innocent, J. Mijoin, P. Magnoux, Applied Catalysis B 75 (2007) 139–146.
[4] J.-M. Giraudon, A. Elhachimi, G. Leclercq, Applied Catalysis B 84 (2008) 251–261.
[5] D.P. Debecker, F. Bertinchamps, N. Blangenois, P. Eloy, E.M. Gaigneaux, Applied Catalysis B 74 (2007) 223–232.
[6] E. Finocchio, G. Ramis, G. Busca, Catalysis Today 169 (2011) 3–9.
[7] E. Finocchio, C. Pistarino, P. Comite, E. Mazzei Justin, M. Baldi, G. Busca, Studies in Surface Science and Catalysis 142 (2002) 967–974.
[8] E. Finocchio, G. Sapienza, M. Baldi, G. Busca, Applied Catalysis B 51 (2004) 143–148.
[9] S. Pitkäaho, S. Ojala, T. Maunula, A. Savimaki, T. Kinnunen, R.L. Keiski, Applied Catalysis B 102 (2011) 395–403.
[10] E. Finocchio, C. Pistarino, S. Dellepiane, B. Serra, S. Braggio, M. Baldi, G. Busca, Catalysis Today 75 (2002) 263–267.
[11] R. López-Fonseca, J.I. Gutiérrez-Ortiz, M.A. Gutiérrez-Ortiz, J.R. González-Velasco, Journal of Catalysis 209 (2002) 145–150.
[12] J.R. González-Velasco, R. López-Fonseca, A. Aranzabal, J.I. Gutiérrez-Ortiz, P. Steltenpohl, Applied Catalysis B 24 (2000) 233–242.

[13] B. de Rivas, R. López-Fonseca, C. Jiménez-González, J.I. Gutiérrez-Ortiz, Chemical Engineering Journal 184 (2012) 184–192.
[14] B. de Rivas, R. López-Fonseca, C. Jiménez-González, J.I. Gutiérrez-Ortiz, Journal of Catalysis 281 (2011) 88–97.
[15] B. de Rivas, J.I. Gutiérrez-Ortiz, R. López-Fonseca, J.R. González-Velasco, Applied Catalysis A 314 (2006) 54–63.
[16] J.I. Gutiérrez-Ortiz, B. de Rivas, R. López-Fonseca, J.R. González-Velasco, Applied Catalysis B 65 (2006) 191–200.
[17] B. de Rivas, J.I. Gutiérrez-Ortiz, R. López-Fonseca, J.R. González-Velasco, Journal of Molecular Catalysis A 278 (2007) 181–188.
[18] Q.G. Dai, X.Y. Wang, G.Z. Lu, Applied Catalysis B 81 (2008) 192–202.
[19] Q.G. Dai, H. Huang, Y. Zhu, W. Deng, S.X. Bai, X.Y. Wang, G.Z. Lu, Applied Catalysis B 117–118 (2012) 360–368.
[20] H.F. Li, G.Z. Lu, Q.G. Dai, Y.Q. Wang, Y. Guo, Y.L. Guo, Applied Catalysis B 102 (2011) 475–483.
[21] X.Y. Wang, Q. Kang, D. Li, Applied Catalysis B 86 (2009) 166–175.
[22] Y. Zhang-Steenwinkel, L.M. van der Zande, H.L. Castricum, A. Bliek, Applied Catalysis B 54 (2004) 93–103.
[23] Y. Yang, Y.B. Sun, Y.S. Jiang, Materials Chemistry and Physics 96 (2006) 234–239.
[24] S. Kumar, Y. Teraoka, A.G. Joshi, S. Rayalu, N. Labhsetwar, Journal of Molecular Catalysis A 348 (2011) 42–54.
[25] V. Szabo, M. Bassir, A. Van Neste, S. Kaliaguine, Applied Catalysis B 37 (2002) 175–180.
[26] H. Najjar, H. Batis, Applied Catalysis A 383 (2010) 192–201.
[27] W.P. Stege, L.E. Cadús, B.P. Barbero, Catalysis Today 172 (2011) 53–57.
[28] D. Kießling, R. Schneider, P. Kraak, M. Haftendorn, G. Wendt, ChemTech 47 (1995) 199–204.
[29] D. Kießling, R. Schneider, P. Kraak, M. Haftendorn, G. Wendt, Applied Catalysis B 19 (1998) 143–151.
[30] G. Sinquin, C. Petit, S.J. Libs, P. Hindermann, A. Kiennemann, Applied Catalysis B 32 (2001) 37–47.
[31] J.A. Alonso, M.J. Martínez-Lope, M.T. Casais, J.L. MacManus-Driscoll, P.S.I.P.N. de Silva, L.F. Cohen, M.T. Fernández-díaz, Journal of Materials Chemistry 7 (1997) 2139–2144.
[32] B.L. He, Q. Song, Q. Yao, Z.W. Meng, C.H. Chen, Korean Journal of Chemical Engineering 24 (2007) 503–507.
[33] S. Royer, H. Alamdari, D. Duprez, S. Kaliaguine, Applied Catalysis B 58 (2008) 273–288.
[34] A. Baylet, S. Royer, C. Labrugère, H. Valencia, P. Marécot, J.M. Tatibouët, D. Duprez, Physics Chemistry Chemical Physics 10 (2008) 5983–5992.
[35] L. Lisi, G. Bagnasco, P. Ciambelli, S. De Rossi, P. Porta, G. Russo, M. Turco, Journal of Solid State Chemistry 146 (1999) 176–183.
[36] J.G. Deng, H.X. Dai, H.Y. Jiang, L. Zhang, G.Z. Wang, H. He, C.T. Au, Environmental Science & Technology 44 (2010) 2618–2623.
[37] H. Ziaei-Azad, A. Khodadadi, P. Esmaeilnejad-Ahranjani, Y. Mortazavi, Applied Catalysis B 102 (2011) 62–70.
[38] L.H. Zhang, F.B. Zhang, N. Wang, R.R. Chen, A.T. Hsu, International Journal of Hydrogen Energy 37 (2012) 1272–1279.
[39] M. Alifanti, J. Kirchnerova, B. Delmon, Applied Catalysis A 245 (2003) 231–243.
[40] R. Hammami, S.B. Aïssa, H. Batis, Applied Catalysis A 353 (2009) 145–153.
[41] M. O'Connell, A.K. Norman, C.F. Hüttermann, M.A. Morris, Catalysis Today 47 (1999) 123–132.
[42] J.C. Carver, G.K. Schweitzer, T.A. Carlson, Journal of Chemical Physics 57 (1972) 973–981.
[43] J.F. Moulder, W.F. Stickle, P.E. Sobol, K.D. Bomben, Handbook of X-ray photoelectron Spectroscopy, Physical Electronics, Inc, Eden Prairie, 1995.
[44] A.F. Carley, M.W. Roberts, A.K. Santra, Journal of Physical Chemistry B 101 (1997) 9978–9983.
[45] J.L.G. Fierro, L. Gonzalez Tejuca, Applied Surface Science 27 (1987) 453–457.
[46] S.H. Liang, T.G. Xu, F. Teng, R.L. Zong, Y.F. Zhu, Applied Catalysis B 96 (2010) 267–275.
[47] H.M. Zhang, Y. Shimizu, Y. Teraoka, N. Miura, N. Yamazoe, Journal of Catalysis 121 (1990) 432–440.
[48] Y.X. Liu, H.X. Dai, Y.C. Du, J.G. Deng, L. Zhang, Z.X. Zhao, C.T. Au, Journal of Catalysis 287 (2012) 149–160.
[49] C.L. Li, Y.C. Lin, Applied Catalysis B 107 (2011) 284–293.
[50] J.J. Zhu, A. Thomas, Applied Catalysis B 92 (2009) 225–233.
[51] R.J.H. Voorhoeve, J.P. Remeika, P.E. Freeland, B.T. Mathias, Science 177 (1972) 353–354.